# Supporting Information

## The potential cytotoxicity and mechanism of $VO_2$ thin films for intelligent thermochromic windows†

Huaijuan Zhou,‡[a, b] Jinhua Li,‡[a, b] Shanhu Bao,[a] Donghui Wang,[a, b] Xuanyong Liu,[a, *] and Ping Jin[a, c, *]

[a] State Key Laboratory of High Performance Ceramics and Superfine Microstructure, Shanghai Institute of Ceramics, Chinese Academy of Sciences, Shanghai 200050, China

[b] University of Chinese Academy of Sciences, Beijing 100049, China

[c] Materials Research Institute for Sustainable Development, National Institute of Advanced Industrial Science and Technology, Nagoya 463-8560, Japan

[*]**Corresponding authors:**

Prof. Ping Jin

State Key Laboratory of High Performance Ceramics and Superfine Microstructure, Shanghai Institute of Ceramics, Chinese Academy of Sciences, Shanghai 200050, China

E-mail: p-jin@mail.sic.ac.cn

Tel.: +86 21 6990 6208.

Fax: +86 21 6990 6221.

Prof. Xuanyong Liu

State Key Laboratory of High Performance Ceramics and Superfine Microstructure, Shanghai Institute of Ceramics, Chinese Academy of Sciences, Shanghai 200050, China

E-mail: xyliu@mail.sic.ac.cn

Tel.: +86 21 52412409.

Fax: +86 21 52412409.

† Electronic Supplementary Information (ESI) available: Additional experimental details and relevant analysis. See DOI:

‡ These authors contributed equally to this work.

# 1. Experimental details

## 1.1. Fabrication of specimens

In brief, $VO_2$ films were deposited through reactive sputtering of 3-inch $VO_2$ ceramic target with Ar content of 50 sccm at DC power of 80 W. Before $VO_2$ films growth process, the deposition chamber was pumped down to ~$10^{-4}$ Pa and pure Ar gas (purity, 99.999%) was introduced. During the deposition process, the substrates were kept at 450 ºC for the fine crystallinity of $VO_2$ films and rotated along the vertical axis at a speed of 10 rpm to improve the film homogeneity. After the $VO_2$ films were deposited, samples were cooled down spontaneously to ambient temperature.

## 1.2 Assessment of energy-saving effect

The optical transmittance characteristics were monitored by the UV−Visible−NIR spectrophotometer (Hitachi U-4100) equipped with an attachment to control the temperature of the films. The temperature was measured precisely with a PT100 temperature sensor in contact with the surface of films, and it was controlled via the temperature controlling unit. The transmittance spectra were collected from 350 nm to 2600 nm and the transmittance curve of the bare quartz was used as a baseline calibration for the transmittance measurements. Hysteresis loops were measured by collecting the transmittance spectra of samples at the fixed wavelength of 2000 nm with a heating-cooling rate of 2.0 °C /min. The integrated luminous transmittance ($T_{lum}$, 380-780 nm) and solar spectrum transmittance ($T_{sol}$, 350-2600 nm) can be acquired from the recorded spectra using the following equation:

$$T_{\rho}=\int \psi_{\rho}(\lambda)T(\lambda)d\lambda / \int \psi_{\rho}(\lambda)d\lambda \quad (1)$$

where $T(\lambda)$ denotes the transmittance at wavelength $\lambda$, $\rho$ means lum or sol, $\psi_{lum}$ is the standard luminous efficiency function for photopic vision, and $\psi_{sol}$ is the solar irradiance spectrum for air mass 1.5 (corresponding to the sum positioned 37$^{o}$ above the horizon).[1]

### 1.3 Zeta potential measurements

In the streaming potential measurements, electrolyte solution was forced (pumped) to flow along solid surfaces (**Scheme S1a**) and the potentials resulting from the motion of ions in diffusion layer were measured according to Helmholtz-Smoluchowski equation,

$$\zeta = \frac{dU}{dP} \times \frac{\eta}{\varepsilon \times \varepsilon_0} \times K$$

in which, $\zeta$ is the zeta potential, $dU/dP$ represents the slope of streaming potential *versus* pressure, and $\eta$, $\varepsilon_0$, $\varepsilon$ and $K$ denote the electrolyte viscosity, vacuum permittivity, dielectric constant of the electrolyte and conductivity respectively. **Scheme S1b** illustrates the schematic diagram of electric double layer in zeta potential measurements. During the measurement process, the information of aforementioned parameters was collected by SurPASS control and evaluation software, and the obtained final zeta potential ($\zeta$) value resulted from SurPASS control and evaluation software treating with parameters ($\eta$, $\varepsilon_0$, $\varepsilon$ and $K$) automatically.

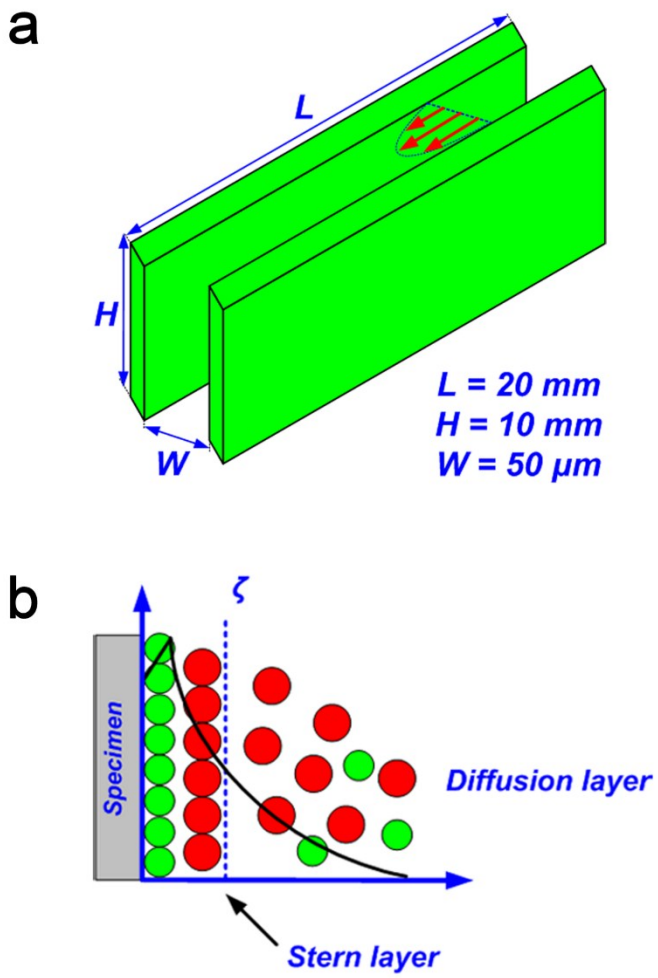


**Supplementary Scheme S1.** Schematic diagrams of the parallel sample holders with double-sided adhesive tape (a) and the electric double layer (b) in zeta potential measurement. The Stern layer is the layer of counter ions (green ions in **Scheme S1b**) that attach to a charged surface. Ion concentration near the charged surface decreases far from the surface, thus generating the Diffusion layer. The zeta potential will be formed when a liquid is forced to flow directly through a small gap produced by two sample surfaces (**Scheme S1a**), thus removing the charge carriers bound in the electric double layer. The zeta potential (ζ) is defined directly at the interface between the Stern layer and the Diffusion layer in **Scheme S1b**.

**1.4 Cell culture**

The human intrahepatic biliary epithelial cells (HIBEpiC) were firstly maintained in the media provided by suppliers in a humidified atmosphere of 5% $CO_2$ at 37 °C and then passaged at a ratio of 1:2~1:3 every 2~4 days according to the cell condition. HIBEpiC were cultured in Epithelial Cell Medium (EpiCM, ScienCell), which was supplemented with 10% FBS (fetal bovine serum) and 1% P/S (Penicillin-Streptomycin) prior to use.

Cellular reducing conditions are known indicators of cell viability and cell death. AlamarBlue reagent functions as a cell health indicator by using the reducing power of living cells to quantitatively measure the cell proliferation and viability of various human and animal cell lines, bacteria, plant, and fungi, which allows to establish relative cytotoxicity of various chemical agents. When cells are alive, they maintain a reducing environment within the cytosol. Resazurin, the active ingredient of AlamarBlue reagent, is a non-toxic, cell permeable compound that is blue in color and virtually non-fluorescent. Upon entering cells, resazurin is reduced to resorufin, a compound that is red in color and highly fluorescent. Viable cells continuously convert resazurin to resorufin, increasing the overall fluorescence and color of the media surrounding cells. The operation procedures and calculation of cell proliferation/viability followed the instruction of the AlamarBlue assay.

## 2. Supplementary analysis

The transmittance of $VO_2$ films in low-temperature monoclinic phase (measured at 25 $^oC$) and high-temperature rutile phase (measured at 90 $^oC$) are exhibited in **Figure S1a**. All of the three films showed an obvious transmittance contrast between the two phases in the near-infrared region, which is attributed to the thermochromic nature of $VO_2$. The plasma frequency ( $\omega_p$ ) for metallic state $VO_2$ is reported to be 1.0 eV (~ 1240 nm)[2] or 1.6 eV (~ 775 nm),[3] thus the rutile phase has a lower transmittance in the IR region since the incident light at a frequency below the plasma frequency leads to motion in the charge carriers that acts to screen out the incident field, in other words, to reflect the incident waves.

By heating up and cooling down the films, the thermochromic characteristics are clearly shown in **Figure S1b**. Sample MS-30 with smaller grains exhibited a less intense and less abrupt transition behavior. Conversely, as the grains increased in size, the density of grain boundaries and associated defects diminished leading to a stronger and sharper transition. To investigate the thermochromic characteristics, the SMT temperature ($T_c$, defined as the central temperature of the hysteresis loop) and hysteresis width (representing the abruptness or sharpness of the SMT) are two momentous parameters. The value for MS-30, MS-80 and MS-120 were 63 $^oC$, 66.5 $^oC$ and 66.8 $^oC$, respectively, as clearly depicted in **Figure S1c**. Such a phenomenon of SMT temperature dependent on film thickness has been reported everywhere.[4] Compared to the $T_c$ of 68 $^oC$ for $VO_2$ bulk single crystal,[5] the three SMT temperatures were somewhat depressed. Although the $T_c$ can be depressed in a variety of approaches (doping, under-

or over-stoichiometry, special structure[6]), the predominant reasons here were believed to be attributed to the crystallinity of the films and the inevitable stress. For MS-30 with small grain size, an increased number of atoms distributed randomly at grain boundaries and a large surface/interface ratio may damage the zigzag chains of the V–V pairs characteristic of the semiconductor phase, leading to the destabilization of the low temperature phase and therefore the decrease of $T_c$. For all the three films, the total stress in the film, as a combination of thermal stress (tensile) caused by the difference in thermal expansion coefficients between film and substrate and the internal stress (compressive) produced by the ion bombardment effect during the film growth, also causes a reduction in $T_c$ value.

The luminous efficiency and solar efficiency, as shown in **Table S1**, were two powerful parameters to assess the energy-saving effects of thermochromic materials in terms of 'smart windows'. With the increment of film thickness, the solar efficiency (the difference in $T_{sol}$ between the R and M phases, $\Delta T_{sol}$) was improved from 5.7% to 13.3 %. Furthermore, a max $\Delta T_{lum}$ (the difference in $T_{lum}$ between the two phases) of 3.3% was achieved in the MS-80 sample. One can note that the MS-30 had a negative value of $\Delta T_{lum}$. In effect, the threshold value of $VO_2$ thickness for the $T_{lum}$ is 50 nm, which was in detail deported in Reference [7]. Below 50 nm, the M phase exhibits lower $T_{lum}$ than does the R phase, while the relationship is reversed above 50 nm. In particular, $T_{lum}$ even slightly increases with thickness in the range of 50 - 80 nm for the M phase, leading to a maximum $\Delta T_{lum}$ at 80 nm.

To evaluate the application performance, $VO_2$ films were deposited on the 400 ×

400 $mm^2$ area of quartz glass and then adopted in a model house to roughly survey the regulation effect of infrared light. The photo of the simulating house was clearly exhibited in **Figure S1e**. The house is made of some boards (15 mm thickness) and its steric size is about $8.5 \times 10^7$ $mm^3$ (550 ×360 × 430 $mm^3$). For fear of heat exchange, both sides of the boards were painted by thermal insulating materials. On the right side, the glass deposited with the $VO_2$ film was placed in front of the house as the window, and the combination of the house and the window was sealed during the testing process. On the left side, a house with a piece of blank glass was served as a control group at the identical test condition. Two infrared lamps (Philips, R125 IR R 150 W) irradiated the house, while two thermoelectric couples were employed to monitor the temperature changes. At the meantime, two InGaAs PIN photodiodes (Hamamatsu Co., G8373-01), which are installed in the small pores in the center of back panel of each model house, sensed the variation in transmittance of infrared lights. At the initial stage, the experimental was carried out at the temperature of 19 $^oC$ in static air. After irradiation for 60 min, as shown in **Figure S1f,** the employment of 120 nm $VO_2$-covered glass resulted in a temperature drop of 9 $^oC$ compared with the bare glass (42 $^oC$). The infrared shielding also ability can be illustrated by the curves of the transmittance of infrared light dependence on irradiation time, which was shown in **Figure S1d**. In response to irradiation time from 0 to 2 min, the transmittance of infrared light for sample MS-30, MS-80 and MS-120 was cut down from 100 % to ~ 53%, 32 % and 18 %, respectively. Afterwards, the transmittance of infrared light was almost constant value.

## Supplementary Data

**Table S1**. The solar energy control properties of $VO_2$ films with three thicknesses.

| Sample | $T_{sol-L}$(%) | $T_{sol-H}$(%) | $\Delta T_{sol}$ (%) | $T_{lum-L}$(%) | $T_{lum-H}$(%) | $\Delta T_{lum}$ (%) | $\Delta T_{2000}$(%) |
|---|---|---|---|---|---|---|---|
| MS-30 | 67.6 | 61.9 | 5.7 | 61 | 63.7 | -2.7 | 43.6 |
| MS-80 | 40.2 | 30.8 | 9.4 | 39.6 | 36.3 | 3.3 | 54.9 |
| MS-120 | 33.5 | 20.2 | 13.3 | 29 | 26.6 | 2.4 | 50.6 |

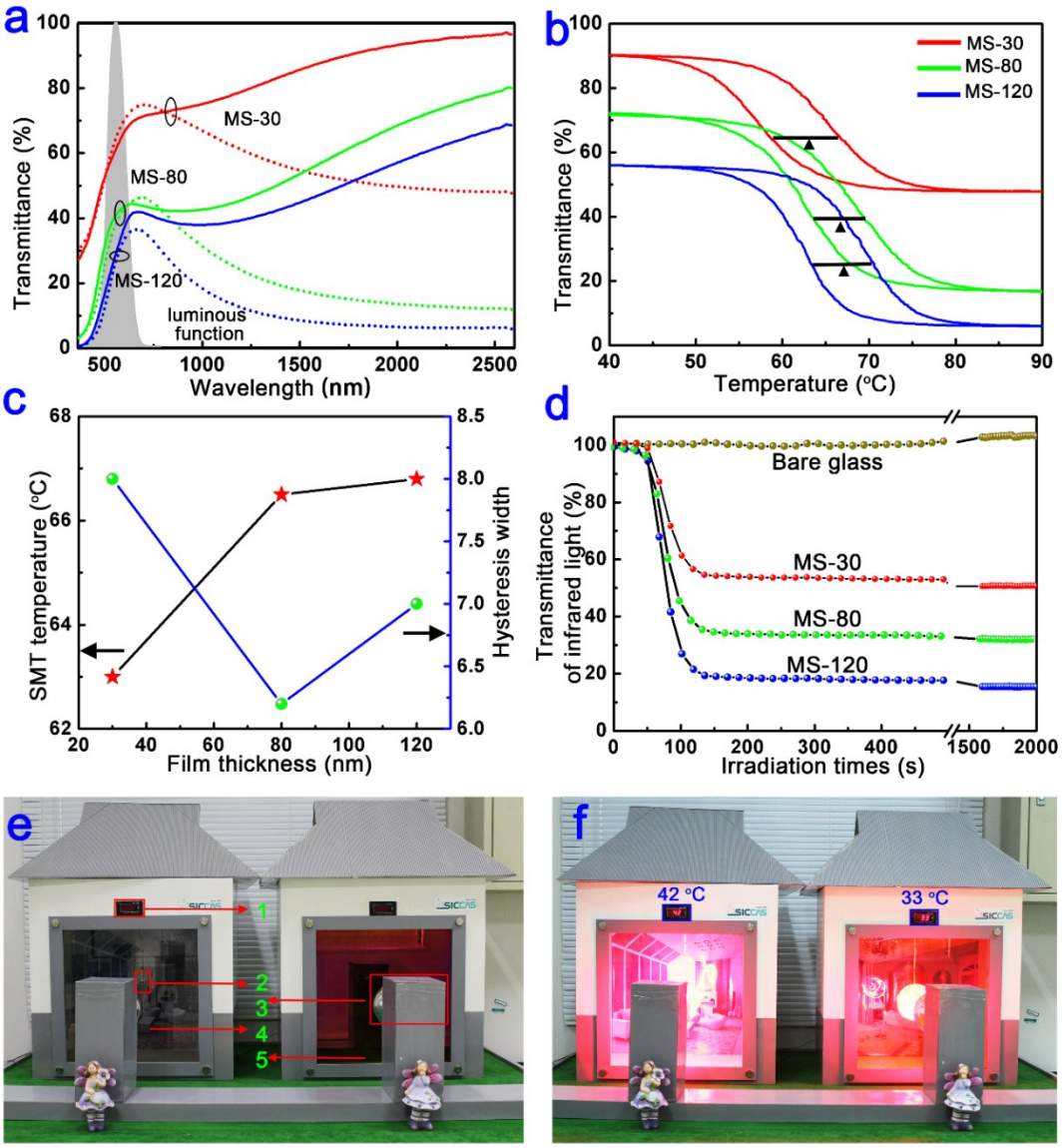


**Supplementary Figure S1.** (a) Optical transmittance spectra of $VO_2$ films. (b) Thermal hysteresis loops of the optical transmittance of the $VO_2$ films at a fixed wavelength of 2000 nm. (c) The SMT temperature and hysteresis width dependence on film thickness. (d) Transmittance of infrared light dependence on irradiation time for sample MS-30, MS-80 and MS-120. (e) Photographic illustration of the model house without irradiation: 1, temperature monitor; 2, temperature probe; 3, infrared lamps; 4, bare glass; and 5, glass deposited with $VO_2$ film of 120 nm. (f) Photograph of model house after irradiation with infrared lamps for 60 min.

## 3. Cell respiration

The cellular respiration can be divided into three metabolic processes, namely, glycolysis, TCA cycle, and oxidative phosphorylation. Each of them occurs in a specific region of the cell.

**(i) Glycolysis.** This is a metabolic pathway that occurs in the cytosol of cells. This pathway can function with or without the presence of oxygen. In a human body, aerobic conditions generate pyruvate and anaerobic conditions form lactate. In aerobic conditions, the process converts one molecule of glucose into two molecules of pyruvate (pyruvic acid), producing energy in the form of 2 net molecules of ATP. In glycolysis, four molecules of ATP per glucose are actually formed, but two are consumed as part of the preparatory phase. The initial phosphorylation of glucose is essential to strengthen its reactivity (weaken its stability) for the molecule to be cleaved into two pyruvate molecules by the enzyme aldolase. During the pay-off phase of glycolysis, four phosphate groups are transferred to ADP by substrate-level phosphorylation to produce four ATP, and two NADH are generated when the pyruvate are oxidized. The overall reaction can be expressed as follow:

$$\begin{aligned} &\text{glucose} + 2\text{NAD}^+ + 2\text{P}_\text{i} + 2\text{ADP} \rightarrow \\ &2\text{pyruvate} + 2\text{NADH} + 2\text{ATP} + 2\text{H}^+ + 2\text{H}_2\text{O} \end{aligned} \tag{S1}$$

Starting with glucose, one ATP is consumed to donate a phosphate to glucose to form glucose 6-phosphate. Glycogen can also be converted into glucose 6-phosphate with the help of glycogen phosphorylase. During energy metabolism, glucose 6-phosphate becomes fructose 6-phosphate. One additional ATP is consumed to phosphorylate fructose 6-phosphate into fructose 1,6-disphosphate with the help of

phosphofructokinase. One fructose 1,6-diphosphate molecule then splits into two phosphorylated molecules with three carbon chains, which later degrades into pyruvate.

**(ii) The TCA cycle.** This process is also called the Krebs cycle or the tricarboxylic acid cycle, which occurs in the matrix of mitochondria. When oxygen is present, acetyl-CoA is generated from the pyruvate molecules produced from glycolysis, and the mitochondria will carry out aerobic respiration which results in the TCA cycle. If oxygen is absent, however, the fermentation of pyruvate molecule will occur. In the presence of oxygen, when acetyl-CoA is formed, this molecule then enters the TCA cycle inside the mitochondrial matrix, and gets oxidized to $CO_2$ while at the same time reducing NAD to NADH. NADH can be used by the electron transport chain to produce further ATP as part of oxidative phosphorylation. To thoroughly oxidize the equivalent of one glucose molecule, two acetyl-CoA must be metabolized by the TCA cycle. Two waste products, $H_2O$ and $CO_2$, are formed during this cycle.

The TCA cycle is an 8-step process involving different enzymes and co-enzymes. During this cycle, acetyl-CoA (2 carbons) plus oxaloacetate (4 carbons) yields citrate (6 carbons), which is rearranged to a more reactive form called isocitrate (6 carbons). Isocitrate is modified to become α-ketoglutarate (5 carbons), succinyl-CoA, succinate, fumarate, malate, and finally, oxaloacetate. The net gain of high-energy compounds from one cycle is 3 NADH (reduced form of nicotinamide-adenine dinucleotid), 1 FADH2 (reduced flavin adenine dinucleotide), and 1 GTP (guanosine triphosphate); the GTP may be subsequently used to produce ATP. Thus, the total yield from 1 glucose molecule (2 pyruvate molecules) is 6 NADH, 2 FADH2, and 2 ATP.

**(iii) Oxidative phosphorylation.** This process is carried out on the inner mitochondrial membrane via the electron transport chain. When glucose is oxidized during glycolysis and the TCA cycle, the co-enzymes $NAD^+$ and FAD are reduced to NADH + $H^+$ and $FADH_2$. In the mitochondria, the electrons from NADH + $H^+$ are transferred to the electron carrier proteins, and the protons are transferred across the membrane. As the electrons move from cytochrome to cytochrome, down the electron transport chain, more protons are carried across the membrane. Cytochrome *c* transfers electrons to the cytochrome *c* oxidase complex. Protons are also transferred to the outside of the membrane by the cytochrome *c* oxidase complex. The cytochrome oxidase complex then transfers electrons from cytochrome *c* to oxygen, the terminal electron acceptor, and water is formed as the product. The transfer of protons generates a proton motive force across the membrane of the mitochondrion. Since membranes are impermeable to ions, the protons that reenter the matrix pass through special proton channel proteins called ATP synthase. The energy derived from the movement of these protons is used to synthesize ATP from ADP and phosphate. Formation of ATP by this mechanism is referred to as oxidative phosphorylation.[8, 9]

## References


1. *ASTM G173 - 03(2012)*.
2. M. Kang, S. W. Kim, J.-W. Ryu and T. Noh, *AIP Advances*, 2012, **2**, 012168.
3. B. Felde, W. Niessner, D. Schalch, A. Scharmann and M. Werling, *Thin Solid Films*, 1997, **305**, 61-65.
4. Z. Luo, X. Zhou, D. Yan, D. Wang, Z. Li, C. Yang and Y. Jiang, *Thin Solid Films*, 2014, **550**, 227-232.
5. F. J. Morin, *Physical Review Letters*, 1959, **3**, 34-36.
6. H. Zhou, J. Li, Y. Xin, X. Cao, S. Bao and P. Jin, *Journal of Materials Chemistry C*, 2015, **3**, 5089-5097.
7. G. Xu, P. Jin, M. Tazawa and K. Yoshimura, *Japanese Journal of Applied Physics Part 1-Regular Papers Short Notes & Review Papers*, 2004, **43**, 186-187.
8. P. Mitchell, *Biochimica et Biophysica Acta (BBA) - Bioenergetics*, 2011, **1807**, 1507-1538.
9. P. Mitchell, *Biological Reviews*, 1966, **41**, 445-501.